Refining aerosol optical depth retrievals over land by constructing the relationship of spectral surface reflectances through deep learning: application to Himawari-8

Tianning Su[1], Istvan Laszlo[2,1], Zhanqing Li[1], Jing Wei[1], Satya Kalluri[2]

[1]Department of Atmospheric and Oceanic Science and ESSIC, University of Maryland, College Park, Maryland 20740, USA

[2]Center for Satellite Applications and Research, NOAA/NESDIS, College Park, Maryland 20740, USA

Abstract

For the past two decades, quantitative retrievals of aerosol optical depth (AOD) have been made from both geostationary and polar-orbiting satellites, and the results have been widely used in numerous studies. Despite the progress made in improving the accuracy of AOD retrievals, there are still major challenges, especially over land. A notable one for the so-called Dark-Target (DT) algorithms is building the surface reflectance (SR) relationships (SRR) to derive SR in the visible channels from SR in the short-wave infrared (SWIR) channel, mainly because these relationships are strongly subjected to entangled factors (e.g., viewing geometry, surface type, and vegetation state). In this study, we examine the benefits of a new method for deriving the SRR using deep learning techniques. The SRR constructed by the deep neural network (DNN) considers multiple related inputs, such as the SWIR normalized difference vegetation index ($NDVI_{SWIR}$), viewing geometry, and seasonality, among others. We then incorporate the DNN-constrained SRR into a DT algorithm developed at NOAA/STAR to retrieve AOD from the Advanced Himawari Instrument (AHI) onboard the new generation of geostationary satellites, Himawari-8. The revised DT algorithm with the deep learning technique (DTDL) demonstrates improved performance over the study region (95–125°E, 18–30°N, a portion of the AHI full disk), as attested by significantly reduced random noise, especially for low $NDVI_{SWIR}$ and high surface albedo cases. Robust independent tests indicate that this algorithm can be applied to untrained regions, not only to those used in training. The method directly benefits the algorithm development for Himawari-8 and can also be adopted for other

geostationary or polar-orbiting satellites. Our study illustrates how artificial intelligence could significantly improve AOD retrievals from multi-spectral satellite observations following this new approach.

1. Introduction

Aerosols critically impact Earth's climate through modulating the energy budget and cloud properties and serve as the primary source of uncertainties to quantifications and interpretations of the changing radiation budget of Earth (Ackerman et al., 2004; Boucher et al., 2013; Chung et al., 2012; Guo et al., 2017, 2019; Li et al., 2011, 2017; Ramanathan et al., 2001). To qualitatively and quantitatively understand aerosols' impact on the climate system, measuring aerosol optical properties using advanced remote sensing techniques is increasingly needed (Kahn et al., 2017; King et al., 2003; Pavlov et al., 2018; Su et al., 2020a; Wei et al., 2018). Among these properties, aerosol optical depth (AOD) is the critical and most widely used product to tackle both scientific questions and air quality monitoring (Chu et al., 2002; Guo et al., 2020; Li et al., 2015; Lin et al., 2015; Su et al., 2017, 2020b; van Donkelaar et al., 2006; Wei et al., 2019a, b). This task is especially important and challenging over land due to the complexity of underlying land properties and aerosol types (Gupta et al., 2016; Levy et al., 2005; Li et al., 2009).

During the last 20 years, substantial progress has been made in aerosol remote sensing techniques for satellites, which is considered the best way to obtain long-term, large-scale AOD products (Colarco et al., 2010; King et al., 1999; Li et al., 2009). Launched onboard Terra (1999) and onboard Aqua (2002), the Moderate Resolution Imaging Spectroradiometer (MODIS) has offered benchmark global AOD retrievals over a long period, which have been extensively used in numerous studies (Gupta et al., 2016, 2018, 2019; Han et al., 2020; 2018; Kaufman et al., 2005; Levy et al., 2007a; Li et al., 2013; Lin et al., 2016; Remer et al., 2008; Su et al., 2018; Wei et al., 2019c, 2020; Yu et al., 2006). Following the success of MODIS, measurements from multiple geostationary and polar-orbiting satellites have been used to retrieve AOD at regional and global scales (Kahn et al., 2009; Laszlo, 2018; Laszlo et al., 2008, 2020; Yoshida et al., 2018).

Several algorithms have been developed to retrieve AOD using data from these sensors, with different merits and weaknesses. A widely used algorithm, the Dark Target (DT) algorithm, has been employed in multiple sensors (Jackson et al., 2013; Kaufman et al., 1997a; Levy et al., 2007b), which has good performance over low albedo regions (e.g., dark ocean and dark vegetated surfaces) (Levy et al., 2013). Another popular algorithm, the Deep Blue (DB) or ultraviolet method, can provide retrievals over bright surfaces with useful accuracy (Hsu et al., 2006, 2013). As a relatively new method, the Multi-Angle Implementation of Atmospheric Correction (MAIAC) has been used to retrieve AOD at the native 1-km resolution with high accuracy (Lyapustin et al., 2011, 2018). Since the DT algorithm was mainly developed for relatively dark regions, the DB and MAIAC algorithms offer higher retrieval rates and more accurate retrievals over bright surfaces due to their different strategies (Hsu et al., 2013; Lyapustin et al., 2018). Among these methods for MODIS, the MAIAC-derived AOD has the best performance (Liu et al., 2019; Mhawish et al., 2019).

The abovementioned algorithms work reasonably well for polar-orbiting satellites, providing long-term AOD products with extensive coverage. However, the temporal resolution for polar-orbiting satellites is limited, while geostationary satellites have great potential to fill this gap (Kim et al., 2008, 2019). An advanced geostationary satellite named Himawari-8 was successfully launched on 7 October 2014 by the Japan Meteorological Agency. As a vital sensor onboard Himawari-8, the Advanced Himawari Imager (AHI) provides spectral reflectance measurements every 10 minutes with variable spatial resolutions of 0.5–2 km at different channels covering Southeast Asia, East Asia, part of South Asia, and Oceania. With high spatial and temporal resolutions, the AHI offers a great opportunity to continuously monitor aerosols over Asia in detail (Gupta et al., 2019). Nevertheless, recent studies have revealed that Himawari-8 AOD products from the Japan Meteorological Agency still suffer from large uncertainties, especially for low Normalized Difference Vegetation Index (NDVI) cases (Wei et al., 2019d; Zhang et al., 2019).

In this study, we focus on improving the DT algorithm, as implemented with Himawari-8/AHI observations at the Center for Satellite Applications and Research (STAR), National Oceanic and Atmospheric Administration (NOAA) (Laszlo et al., 2008, 2018a, 2018b). A core part of the DT algorithms is the estimation of spectral surface reflectances (SR) in the visible channels (0.47/0.64 μm) from SR in the short-wave infrared (SWIR) channel (2.25 μm). The usual way to accomplish this is to use empirical functions to describe the SR relationships (SRR) between the visible and SWIR channels with consideration of the scattering angle and the NDVI at SWIR ($NDVI_{SWIR}$) (e.g., Jackson et al., 2013; Kaufman et al., 1997b; Levy et al., 2007b). Due to the complexity of the SR relationships, such empirical regressions usually lead to relationships fraught with large biases, a major source of uncertainties in AOD retrievals.

Since it appears difficult to establish mathematical functions in closed form that accurately characterize the SRR, deep learning techniques may offer a better way to deal with the task. The multi-layer artificial neural network, a primitive deep learning technique, has been widely employed (Cireşan et al., 2012; Liu et al., 2017; Seide et al., 2011) for a variety of environmental and geographical studies (e.g., Deng and Yu, 2014; Ma et al., 2020; Tong et al., 2019). Hence, we use the multi-layer neural network (i.e., the deep neural network, or DNN) to construct the SRR that accounts for the influences of multiple variables ($NDVI_{SWIR}$, viewing geometry, time, etc.). The DNN-constrained SRR is then incorporated into the NOAA/STAR DT algorithm. The revised DT algorithm with deep learning techniques (DTDL) provides an example of how deep learning could improve retrievals of AOD from multi-spectral satellite observations.

The paper is structured as follows: General information about multi-source data used and preprocessing are presented in Section 2. Section 3 describes the SRR constructed by traditional fitting and by the DNN. Section 4 presents the methodology of the revised algorithm DTDL. The objective of this paper is to test the application of a deep learning technique for deriving SRR and to demonstrate the improvement in AOD retrievals. Therefore, we only present the most relevant features of the algorithm in Section 4. An evaluation of the new algorithm is demonstrated in Section 5. Section 6 presents a summary and concluding remarks.

2. Data and Instruments

2.1. Himawari-8/AHI sensor

The new generation of geostationary satellite Himawari-8 carrying AHI was launched on 7 October 2014 and became operational on 7 July 2015. AHI is able to image East Asia every 30 seconds while offering full-disk coverage of the Pacific region (longitude: 80°E – 160°W, latitude: 60°S – 60°N) every 10 minutes from a geostationary orbit over the equator at ~140°E (https://www.data.jma.go.jp/mscweb/en/product/library_data). Table S1 summarizes the characteristics of the spectral channels of AHI. The NOAA/STAR over-land AOD algorithm uses five shortwave channels (1, 3, 4, 5, and 6) with central wavelengths of 0.47, 0.64, 0.86, 1.61, and 2.25 μm. The nominal spatial resolutions of observations in these channels are, in order, 1, 0.5, 1, 2, and 2 km. To provide consistent inputs, observations from the higher-resolution channels are averaged to the lowest spatial resolution of 2 km, with a temporal resolution of 30 min. Due to the focus of our current project, we obtained AHI data over a specific region (95–125°E, 18–30°N) in 2017 (see Fig. 1). We analyze data from 00:00 to 09:00 UTC, which corresponds to the daytime over the region studied.

2.2. Ground AOD measurements

In this study, we utilize ground-based AOD datasets obtained from two observation networks: the Aerosol Robotic Network (AERONET) and the Chinese Sun–Sky Radiometer Observation Network (SONET). The ground-based observation network of sun and sky scanning radiometer, AERONET, provides aerosol retrievals under clear-sky conditions every 15 min. It is widely utilized to evaluate aerosol retrievals derived from satellites (Giles et al., 2019; Holben et al., 1998; Li et al., 2014). With reported uncertainties of 0.01–0.02, AOD retrievals derived from AERONET are much more accurate than any satellite retrieval (Eck et al., 1999) and have thus been regarded as "ground-truth". Version 3 Level 1.5 AOD products derived from AERONET are used in our study (https://aeronet.gsfc.nasa.gov/). The ground-based CIMEL radiometer network in China, SONET (http://www.sonet.ac.cn/), uses the same instruments and algorithms as used in AERONET, with a similar uncertainty of 0.01–0.02 (Li et al., 2018).

Here, we used data from 16 AERONET sites and 2 SONET sites for cloud-free scenes over the study region (Fig. 1). The AERONET and SONET AOD retrievals are typically available at multiple wavelengths (i.e., 440, 500, 675, 870, and 1020 nm). Following Eck et al. (1999), a quadratic fit is used to characterize the relationship between the logarithm of AOD and the logarithm of wavelength. The AOD at 550 nm is then interpolated, based on the relationship between AOD and wavelength. The ground-based AODs at 550 nm are used in two ways. They provide the AOD input needed to estimate the SR from which the SRR is built (see Section 3.1). They are also the source of "ground-truth" in the evaluation of AHI-retrieved AOD (see Section 5).

2.3. Auxiliary data

An external cloud mask serves as input for identifying clear-sky pixels for both establishing the SRR and aerosol retrievals. The external cloud mask (Heidinger et al., 2016) is produced upstream to the AOD retrieval, and as such, it is not part of the AOD algorithm. The cloud mask is processed at the same temporal and spatial resolutions as the AHI measurements. Note that the presence of cirrus clouds in a scene is usually detected by the 1.38-µm channel in other satellites (Gao et al., 1995, 2002). Due to the lack of a 1.38-µm channel on AHI, cirrus is primarily identified by the 11- and 12-µm split-window test. We note that other methods also exist for detecting cirrus in an AHI pixel. For example, Imai and Yoshida (2016) developed a CO_2 slicing technique. We also use the land/ocean mask to choose the appropriate algorithm (land or ocean) for retrieving AOD.

Total amounts of water vapor and ozone, surface wind field, pressure, and surface altitude are obtained at a horizontal resolution of 0.5°×0.5° from the National Centers for Environmental Prediction Global Forecast System (GFS) model data at a 3-hr interval (https://www.nco.ncep.noaa.gov/pmb/products/gfs/). These data are interpolated to match the uniform spatial resolution of 2 km and the temporal resolution of 30 min of the AHI reflectance data. In particular, model data are linearly interpolated to match the times of satellite observations. For a given satellite pixel, we use the model data closest to the pixel. The temporal and spatial resolutions of GFS data are coarser than those of the satellite data. Thus, interpolation inevitably leads to some uncertainties. Note that the model itself also suffers from considerable uncertainties. However, since observations are not available everywhere, the only feasible option is using model or reanalysis data.

3. Spectral surface reflectance relationships

SR estimated by SRR is one of the most important factors affecting the accuracy of AOD retrievals over land (Kaufman et al., 1997b; Levy et al., 2007b). Similar to the DT algorithm for MODIS (Remer et al., 2005), the National Environmental Satellite, Data, and Information Service/STAR DT algorithm (Laszlo et al., 2018a) retrieves SR (simultaneously with AOD) using empirical relationships between the SRs in the blue (0.47 μm), red (0.64 μm), and SWIR (2.25 μm) bands of dark, dense vegetation. Kaufman et al. (1997b) explained that the existence of such relationships is the result of the correlation between chlorophyll (which absorbs radiation in the red/blue band) and liquid water (which absorbs radiation in the SWIR band).

The estimation of spectral SR needed to build the relationships is described next. This is followed by showing "traditional" regression-based relationships and an improved relationship derived by applying a deep neural network.

3.1. Estimation of SR

SRs at 0.47, 0.64, and 2.25 μm needed to determine the relationships between them are estimated from the AHI reflectances by accounting for atmospheric effects. Following Vermote et al. (1997a), we use the NOAA/STAR DT AOD algorithm that calculates the surface and atmospheric contributions to the top-of-the-atmosphere (TOA) reflectance. Assuming a Lambertian surface, contributions of the surface (ρ_{surf}) and atmosphere (ρ_{atm}) to the TOA reflectance (ρ_{toa}) are calculated as (Vermote et al., 1997a, 1997b):

$$\rho_{surf} = T^{O_3}T^{og}T^{H_2O}\left[T_{R+A}T_{R+A}\frac{\rho_{lam}}{1-S_{R+A}\rho_{lam}}\right] \tag{1}$$

$$\rho_{atm} = T^{O_3}T^{og}\left[\left(\rho_{R+A}-\rho_R(P_0)\right)T^{\frac{1}{2}H_2O}+\rho_R(P)\right] \tag{2}$$

$$\rho_{toa} = \rho_{atm} + \rho_{surf} \tag{3}$$

where T^{og} indicates the transmittance from absorption contributed by gases other than water vapor and ozone; T^{O_3} represents the transmittance from ozone absorption; T^{H_2O} and $T^{\frac{1}{2}H_2O}$ are the transmittances from total and half column water vapor absorption, respectively; T_{R+A}/T_{R+A} indicate the total (i.e., direct plus diffuse) downward/upward atmospheric transmissions; S_{R+A} represents the atmospheric spherical albedo; $\rho_R(P)$ represents the Rayleigh reflectance contributed by molecular scattering at the real surface pressure (P); ρ_{R+A} represents the path reflectance by molecules and aerosols at the standard surface pressure (P_0); and ρ_{lam} is the Lambertian land surface reflectance. When everything needed to calculate ρ_{atm} is known, ρ_{surf} is determined from Eq. 3. Equation 2 is then solved for the surface reflectance ρ_{lam}. We apply this process at the AERONET/SONET sites where AOD is known from ground-based measurements.

Radiative properties of aerosols (normalized extinction coefficient, phase function, and single-scattering albedo) required to calculate reflectances and transmittances are currently prescribed by one of four candidate aerosol models (generic, urban, smoke, and dust) identified by the NOAA/STAR DT algorithm as part of the AOD retrieval. We recognize that this aerosol model may not be optimal for two reasons. First, the candidate models only represent broad categories of aerosol properties. For a particular retrieval, the actual property of aerosols likely differs from the property prescribed by any of the candidate models. Second, since the model selection is influenced by the SRR used in the DT algorithm, uncertainties in SRR contribute to the uncertainty in the model selection, especially when the 550-nm AOD is larger than about 0.5, i.e., when the radiative properties of candidate aerosol models differ the most from each other. For the dataset used in this study, this applies to only about 30% of the samples. The approximate threshold of 0.5 applies only for the generic and urban models and for the normalized extinction of the smoke model. Radiative properties of dust and the single-scattering albedo and phase function of smoke are different from those of the generic and urban models, even at optical depths smaller than 0.5. The impact of erroneous model selection is expected to be somewhat mitigated by screening out low-quality retrievals, which, among other factors, are associated with poor agreement between the observed and calculated TOA spectral reflectances, which can happen when the aerosol model picked by the retrieval is likely in error. Even though the calculated SR suffers from multiple sources of uncertainties (e.g., the Lambertian assumption, aerosol optical properties, and aerosol vertical distribution), it is still considered suitable for retrieving AOD because the same assumptions are made in the AOD retrieval. Thus the SRs calculated from Eqs. 1–3 are considered as “ground truth”.

Calculations of T^{H_2O} and T^{O_3} require the column amounts of water vapor and ozone, respectively. These parameters, along with other meteorological parameters needed in Eq. 1, are obtained from the GFS. Laszlo et al. (2018a) provide details of calculations of all gaseous transmittances, including T^{og} and Rayleigh reflectance. In constructing the database used for establishing SRR, all available 2-km SR retrievals are averaged within 10 km around the ground sites.

3.2 SRR from regression

The absorption of liquid water and chlorophyll at visible (e.g., blue or red bands) and SWIR wavelengths are related to the state of the vegetation. The relationships of spectral SR are also affected by the vegetation state, as well as seasonality (Kaufman and Remer, 1994; Kobayashi et al., 2007; Remer et al., 2001). The state of vegetation is usually characterized by the top-of-canopy NDVI. However, because this NDVI requires knowledge of AOD, $NDVI_{SWIR}$ is used as an aerosol-independent measure of the vegetation state, in practice. It is defined as (Levy et al., 2007b):

$$NDVI_{SWIR} = (\rho^m_{1.61} - \rho^m_{2.25})/(\rho^m_{1.61} + \rho^m_{2.25}) \tag{4}$$

where $\rho^m_{1.61}$ and $\rho^m_{2.25}$ are the AHI-measured reflectances at 1.61 μm (channel 5) and 2.25 μm (channel 6), respectively.

Figure 2 presents the scatterplots of $SR_{0.47}$ (Fig. 2a-b) and $SR_{0.64}$ (Fig. 2c-d) as a function of $SR_{2.25}$, with colors representing values of $NDVI_{SWIR}$ (left panels) and scattering angle (right panels). Hereafter, SR_λ represents the SR at wavelength λ (i.e., 0.47, 0.64, and 2.25 μm). Despite the scatter, higher SR is generally associated with lower $NDVI_{SWIR}$ and higher scattering angles. The simplest linear regressions in the form of Y = *m* + *n* X, where *m* and *n* are constants, are also shown. These simple linear regressions cannot fully characterize the SRR between visible and SWIR channels, so it is necessary to add $NDVI_{SWIR}$ and scattering angle into the empirical relationship between SR in multiple channels (Laszlo et al., 2018a; Remer et al., 2013). Table 1 presents the SRR obtained this way and used in this study as one of the possible empirical functions to represent the SRR. The regression coefficients are derived from the least-squares method for multiple parameters (Bühlmann and Van De Geer, 2011).

3.3. SRR from DNN

We adopted the DNN to derive SR at the visible channel (0.64 μm) from SR at the SWIR channel (2.25 μm). The DNN is designed based on the structure and functions of the nervous system and the brain, which can contain a large number of interconnected individual elements (i.e., artificial neurons) working in parallel (Cireşan et al., 2012; Sarle, 1994; Seide et al., 2011). Using a sufficient dataset to train the model, a DNN model can provide a predicted output for new input data due to its learning ability (Schmidhuber, 2015).

Instead of specific functions, we use the DNN to train the relationship between $SR_{0.64}$ and $SR_{2.25}$ based on measurements within 10 km around the AERONET/SONET sites. Based on the previous descriptions and Eqs. 1–3, we add additional inputs, including $NDVI_{SWIR}$, scattering angle, TOA reflectances at 0.47/0.64/2.25 μm, seasonality, column amount of ozone, column amount of water vapor, and the pressure at the surface level. Meteorological parameters are obtained from the NCEP GFS. The seasonality is classified as winter (December–January–February), spring (March–April–May), summer (June–July–August), and autumn (September–October–November). The four seasons are denoted as 1, 2, 3, and 4, respectively. The seasonality is then used in the DNN training and prediction. Due to the nonlinearity in the relationships among various parameters, the DNN model is based on the Bayesian regularization approach for tracking various nonlinear functions (Burden and Winkler, 2008). The maximum number of epochs is set as 10,000 to allow sufficient training. As shown in Fig. 3, the corresponding input data are extracted from a geographical grid. The input data are then interconnected with multiple neurons within the hidden layers. Figure 3 also shows the architecture of neurons in the hidden layers. The total number of hidden layers is n+3, where n can be adjusted as needed. The first and second hidden layers have 8 and 4 neurons, respectively, and the last hidden layer has one neuron. Other hidden layers have two neurons. The neuron is a processing element that sums the inputs and weights. The strengths and importance of the connections are represented by neuron biases and weights, which are automatically adjusted in the training process. The predicted $SR_{0.64}$ would then be generated for a given grid based on the training model.

3.4. The performance of SRR derived from regression and DNN

The performance of the empirical function in the traditional approach is shown in Fig. 4a that plots the 0.64-μm SR estimated from the empirical function as a function of the "true" 0.64-μm SR obtained from the AHI TOA reflectance and the ground-observed AOD using Eqs. 1–3. The plot shows a fair amount of scatter for individual retrievals that could lead to considerable errors in AOD. The empirical function is also likely to underestimate at the high end and overestimate at the low end of the "true" SR values.

For evaluating the performance of the DNN model, we use the sample-based cross-validation (CV) technique (Rodriguez et al., 2010). For the CV process, we randomly choose 70% of the total samples for training, then utilize the remaining 30% of the dataset for validation. Such a procedure is repeated ten times to avoid biases in the selection. Basically, the data sample size for validation is expanded ten times, while the samples do not overlap with the training data. Figures 4b-e present the scatterplots of the 10-CV results of $SR_{0.64}$ for different numbers of hidden layers with the architecture shown in Fig. 3. Samples of 10-CV are three times the original dataset. The number of neurons is a critical parameter in the DNN but does not significantly affect the DNN performance in this study. Despite a slightly larger bias when the number of hidden layers is three, DNN-derived $SR_{0.64}$ shows consistent performance for different numbers of neurons. With the smallest root-mean-square error (RMSE), we set the total number of the hidden layers to 7 and the total number of neurons to 27. In the architecture constructed in our study, the DNN predicts $SR_{0.64}$ with RMSEs and mean absolute errors (MAEs) that are about a third of those predicted by the empirical function, as shown in Fig. 4.

Following previous studies (e.g., Gupta et al., 2016), we still use an empirical linear relationship to calculate $SR_{0.47}$ from $SR_{0.64}$ (Fig. S1). The linear regression predicting $SR_{0.47}$ from $SR_{0.64}$ captures the overall, dominant characteristics of the true $SR_{0.47}$ and results in a relatively good correlation coefficient (0.9). But the residual error of the linear fit is still considerable because of the large scatter in the data.

In the current stage, we do not use the DNN to train the relationship between $SR_{0.47}$ from $SR_{0.64}$ because we found that the DNN may predict unphysical values of $SR_{0.47}$ based on preliminary analyses (e.g., smaller than 0 or larger than 0.3, the maximum value expected for the vegetated surface at this wavelengths). However, we do not rule out the possibility that the DNN may improve the performance of retrieved $SR_{0.47}$ with appropriate inputs and architecture. Based on the linear fitting of SR, we use a simple regression ($SR_{0.47} = 0.86 \times SR_{0.64} - 0.02$) to derive $SR_{0.47}$ from the DNN-derived $SR_{0.64}$. To avoid negative values, $SR_{0.47}$ is set to 0.01 when $SR_{0.64}$ is less than 0.025.

4. Dark-target – Deep-learning (DTDL) algorithm

4.1. The algorithm combining the DNN and the DT method

We implemented the DNN scheme for the SRR into the NOAA/STAR DT algorithm for Himawari-8/AHI. This DT algorithm follows the approach applied to the GOES-R Advanced Baseline Imager and described in more detail by Laszlo et al. (2018a). For this DT algorithm, the land aerosol models are adopted from previous studies for MODIS (Levy et al., 2007a; Remer et al., 2006). Detailed information about these aerosol models can be found in Table S2. There are notable uncertainties in the AOD retrievals associated with assumed aerosol models, which may lead to uncertainties of more than 10% in the retrievals (Jeong et al., 2005; Mielonen et al., 2011; Tirelli et al., 2015; Wang et al., 2017; Wu et al., 2016). This is very difficult to solve since we cannot actually obtain or retrieve the real aerosol model from monodirectional, multispectral intensity measurements alone. Moreover, different types of aerosols are mixed in the real atmosphere and show large vertical variations. Such complex information may not be conveyed by some common aerosol models (Li et al., 2020). Unlike oceans, the surface properties of land demonstrate large variability and great complexity, making modeling the spectral SR difficult. The bias in SR further serves as a major source of uncertainties in the aerosol retrieval over land. The SRR trained by the DNN is expected to mitigate the problem.

The retrieval algorithm can be described as searching for the pair of AOD and SR that leads to calculated TOA reflectances which best fit the observed TOA reflectances at 0.47, 0.64, and 2.25 μm. Instead of directly using a radiative transfer model (i.e., 6SV v1.1), a look-up table (LUT) of necessary terms for several candidate aerosol models, AOD values, and geometries was generated, based on the 6S vector radiative transfer model (Vermote et al., 1997a) for efficient calculations. Figure 5 outlines the procedure of simultaneous AOD retrievals and SR. For each aerosol model, an iterative procedure is presented by looping over the AOD values in the LUT in ascending order. For a specific step i in the loop, a value of $SR_{2.25}$ is calculated from the AOD and the TOA reflectance in the SWIR channel. $SR_{0.64}$ is then directly estimated through the DNN-trained SRR described in Section 3.1.1. $SR_{0.47}$ is calculated from the DNN-derived $SR_{0.64}$, based on linear regression. The TOA reflectance at 0.47-μm ($\rho_{0.47,i}$) is derived from $\tau_{550,i}$ and $SR_{0.47}$. The loop over the AOD values is terminated when $\rho_{0.47,i}$ converges to the observation ($\rho_{0.47}^{obs}$). For the current aerosol model, the AOD retrieval is further estimated based on linear interpolation. Furthermore, the corresponding TOA reflectance at 0.64 μm is calculated from the current AOD retrieval and $SR_{0.64}$. The associated residual is calculated as the squared difference between the observed TOA reflectance and the calculated TOA reflectance at 0.64 μm. By looping the aerosol model, the AOD retrieval is selected as the solution with the smallest residual.

4.2. Quality control

In the NOAA/STAR DT algorithm, several external masks and internal tests are applied to screen out unsuitable pixels and control the quality of AOD retrievals. Details of the procedures are provided by Laszlo et al. (2018a), but here, we summarize the major ones for completeness. First, pixels with $\rho_{0.47}^{obs} > 0.4$ are deemed as cloudy or too bright for the aerosol retrieval and are excluded. An internal snow test and ephemeral water test are then applied, following previous studies (Jackson et al., 2013; Walton et al., 1998). An internal inhomogeneity test is also performed to further screen pixels. Detailed information on these tests is provided in the publicly available algorithm theoretical basis documents referenced by Laszlo et al. (2018a). Based on the retrieval residual, external masks, and internal tests, the AOD retrievals are classified into four quality levels (i.e., no retrieval, low quality, medium quality, and high quality). Following Laszlo et al. (2018a), Table S3 summarizes the criteria for determining the quality level of AOD retrievals. Cases with no retrieval and low quality are excluded in our analyses, including those presented in Section 3.

5. Evaluation of AOD retrievals

5.1. An Overview of AOD retrievals from the DTDL algorithm

After implementing the DTDL algorithm, AOD retrievals at 550 nm were made from Himawari-8/AHI over the study region during the period 1 January 2017 to 31 December 2017 at a 2-km spatial resolution. To isolate the changes in the retrievals caused by the SRR, retrievals from the DTDL algorithm used the same inputs as the DT algorithm. Figure 6a shows the medium- and high-quality AODs that are used in the evaluation. Several polluted regions associated with high population densities are identified with relatively high AOD values, including the Red River Delta, the Sichuan Basin, western Taiwan, and the Pearl River Delta. The available retrieval rate is calculated as the number of available AOD retrievals divided by the total number of samples (~3600), which is around 20% for plains with dense vegetation. It is much lower for arid regions due to the relatively brighter surface (Fig. 6b). The spatial distributions of averaged AOD and retrieval rates during daytime for high-quality AODs are presented in Fig. S2. The AOD pattern is similar for high-quality cases in terms of spatial distribution, but the retrieval rates are generally less than one-third of the total sampling. The DTDL algorithm uses the same framework as the DT algorithm. The retrieval rates of the DTDL and the DT algorithms are thus the same when AOD is not filtered for quality. By contrast, algorithms, like the MAIAC algorithm, that provide retrievals over a wide range of surfaces (Mhawish et al., 2019) are expected to have higher retrieval rates than those of the DTDL algorithm.

We also compare the diurnal variation in AODs retrieved from Himawari-8/AHI measurements and those derived from ground measurements (Fig. 7). These diurnal variations are averaged from data for the year 2017. AHI retrievals matched with ground measurements from 18 sites are used to avoid biases due to sampling differences caused by quality control. The ensemble of all matched data is then used in the analyses of the AOD diurnal variations. In general, aerosol loading based on ground data slightly increases between 00:00–02:00 UTC, reaching a maximum value around 02:00 UTC, and gradually decreasing thereafter. The AHI AOD retrievals derived from the original DT method have a very different diurnal pattern. DT-derived AODs generally decrease until about 02:00 UTC, reaching a maximum around 06:00 UTC. As a result, the largest bias exists around 02:00 UTC when the ground AOD reaches its maximum, and the DT-derived AOD is much lower. However, the mean bias of DT is not always larger than the DTDL bias. For example, it is slightly smaller than that of the DTDL at 05:00 UTC.

The diurnal biases for the original DT and the DTDL algorithms during different seasons are presented in Fig. S3. The considerable mean bias of the DT retrievals around 02:00 UTC is likely caused by the large bias during spring (Fig. S3). After implementing the DTDL method, the systematic biases during spring diminish considerably. The AHI AOD retrievals from the DTDL algorithm show higher consistency with the ground AOD measurements in all seasons. Some features in AOD biases are shared by the original DT and DTDL algorithms, such as the overestimation in AOD retrievals at 00:00 UTC. Such systematic biases need to be considered when using AHI AOD retrievals in this region.

5.2. Validation of AOD retrievals against ground measurements

Figure 8a-b show comparisons between ground-measured AOD and AOD derived from the original DT algorithm for medium-quality and high-quality data. Figure 8c-d show comparisons between ground-measured AOD and AOD derived from the DTDL algorithm. Note that 70% of ground AOD measurements used in model training are excluded from the analysis. The AODs retrieved from the DTDL algorithm are generally improved for both medium-quality and high-quality categories. With the new DTDL algorithm, DNN-based SRR, the uncertainties (represented by the MAE) of the AHI retrievals are reduced by about 30%. Such a significant reduction in noise considerably improves the quality of the AOD product.

The DTDL method is able to produce better AOD retrievals over a region even though the training takes place in another region. Additional independent tests were performed to demonstrate this. The study region was divided into four regions: R1 and R2, defined by latitude, and L1 and L2, defined by longitude (Table 2). We use the dataset from R1 to train the model and validate the results over R2. Such a test is repeated for each region. Figure 9a-d shows comparisons between ground-measured AOD and DT-derived AOD for the four regions. Figure 9e-h shows comparisons between ground-measured AOD and DTDL-derived AOD for R1, R2, L1, and L2, while the training datasets are obtained over regions R2, R1, L2, and L1, respectively. This process ensures the independence of training and validation datasets. Medium-quality and high-quality retrievals are jointly used here. For all four regions, the DTDL-derived AOD shows notable improvement in all three metrics used to measure quality (i.e., correlation coefficient, RMSE, and MAE). The uncertainties of AOD retrievals by DTDL are reduced by 15–25%. The same procedure is performed for high-quality cases, producing similar results (Fig. S4). Thus, the DTDL algorithm not only performs better in regions with training data but also consistently performs better than the traditional DT algorithm over untrained regions.

Regarding the original DT method, the empirical relationship leads to a large bias in estimated SR and can further contribute to the notable uncertainties in AOD retrievals. By implementing a DNN model, multiple contributing factors for the SRR, such as meteorological data and seasonality, can be taken into consideration. The DNN model appears to be a good way to characterize the complex and nonlinear SRR between visible and SWIR channels. The accuracy of AOD retrievals considerably benefits from the improved SRR derived from the DNN. Many factors contribute towards the biases in AOD retrievals, such as surface reflectance, cloud contamination, aerosol model, and aerosol vertical distribution, among others. In this study, we have focused on refining the surface reflectance assumption, but we also bear in mind that other factors can contribute to the error in AOD retrievals.

5.3. Uncertainty related to various factors

Since the quality of satellite AOD retrievals depends on the underlying surface and viewing geometry, we calculate the mean absolute differences between the AOD retrievals from ground measurements and AHI under various conditions. Figure 10 shows the average absolute bias of AOD for different values of $SR_{0.47}$, $SR_{0.64}$,

$NDVI_{SWIR}$, and scattering angle for medium-quality and high-quality retrievals. The mean absolute biases for the original DT and DTDL algorithms are 0.15 and 0.1, respectively. However, the absolute biases in DT-derived AOD can be very large for scenes with a high albedo and low NDVI. This is because the biophysical relationship is valid for dark and dense vegetation but less valid for arid and bright surfaces characterized by low NDVI and a high albedo. Note that the frequency of occurrence of high albedo in the region studied is low. Thus, even relatively few outliers can considerably affect the average calculated from AOD over regions with a high surface albedo.

Compared with the original DT algorithm, the absolute bias of the DTDL algorithm is systematically reduced under various conditions. In Fig. 10, the shaded parts represent standard deviations that are generally larger for the original DT algorithm than for the DTDL algorithm. The traditional DT method cannot deal well with relatively bright surfaces or less vegetated surfaces. Although the DTDL algorithm is also significantly affected by these factors, the revised method can considerably mitigate this issue. The absolute biases of high-quality retrievals as functions of SR, $NDVI_{SWIR}$, and scattering angle are presented in Fig. S5. The pattern of change in biases with these variables is similar to that shown in Fig. 10 for the combined medium- and high-quality retrievals, but the magnitude of the biases is smaller. The DTDL algorithm also produces smaller absolute biases in AOD retrievals at all 18 sites (Fig. S6).

The biases in AOD retrievals are considerably reduced after implementing the DNN-derived SRR in the DTDL algorithm. However, since the visualization of a deep learning model is generally insufficient, interpretability and casualty have been widely recognized as major weaknesses of the DNN (Runge et al., 2015; Zhang et al., 2018), which may be addressed in the future Montavon et al., 2017; Reichstein et al., 2019). Currently, we only compare the original DT and DTDL algorithms in this study since there is no public Himawari-8 AOD product from the other two major methods (DB and MAIAC).

6. Summary

In this paper, we developed a new method (DTDL) that combines the traditional DT approach, as applied in the NOAA/STAR AOD algorithm for AHI, with a deep learning technique (i.e., DNN) to improve estimates of spectral SR needed for AOD retrievals. The core part of the algorithm for retrieving AOD is a radiative transfer model represented by a LUT. The DTDL algorithm still keeps this part (i.e., the LUT) but changes how the surface reflectance is estimated. Due to the complexity of land surface properties, the difficulty in modeling spectral SR constitutes a major source of uncertainties in AOD retrievals in the DT algorithm. The DTDL algorithm applies the DNN to infer the surface albedo at the visible channel and to tackle the nonlinear relationship between multiple, mutually dependent parameters. The improvement in characterizing SRR leads to better AOD retrievals.

One year of the Himawari-8/AHI dataset is employed for the evaluation of the proposed method. The DTDL algorithm demonstrates better performance over the study region, with a ~30% reduction in random noise. AOD retrievals are significantly affected by the albedo and vegetation state of the underlying surface. Low NDVI and high albedo are associated with each other and are two major factors contributing to large biases in AOD retrievals by the DT algorithm. After applying the DNN-derived SRR in the DTDL algorithm, this problem is lessened considerably. Four independent tests are carried out to train and test in different regions to ensure the applicability of the DTDL algorithm. The DTDL algorithm consistently produces better retrievals than the traditional DT algorithm over untrained regions, with a ~20% reduction in uncertainties.

Due to its stability and accuracy, the DTDL algorithm has a large potential for improving aerosol retrievals over land. The comprehensive evaluation provides firm support for our method in the study region. Although this area spans thousands of kilometers, it is still limited to a portion of the AHI full disk. The surface measurements of AOD at the 18 sites under study do not cover all underlying surface conditions. Therefore, the application of the DTDL algorithm to a larger area is warranted to gain a full understanding of the representation and adaptability of this method. The deep learning technique and strategy may also be revised and improved in the future.

As pointed out by Reichstein et al. (2019), a physical scheme and deep learning can be complementary, and their fusion offers great potential for geoscientific analysis. Our study successfully implements this strategy and shows the potential application of such a hybrid method combining the physical approach and deep learning. Our study demonstrates how artificial intelligence could significantly improve AOD retrievals from multi-spectral satellite observations.

Acknowledgements

The project is sponsored by the Taipei Economic and Cultural Representative Office in the United States (TECRO) and the American Institute in Taiwan (AIT) and executed by the Center for STAR of the U.S. NOAA in collaboration with the Central Weather Bureau (CWB) of Taiwan through the Oceanic and Atmospheric Research (OAR) of NOAA. T. Su acknowledges grant CICS EBMC_SIAQ-18 provided to the University of Maryland by NOAA to execute part of the TECRO project. We appreciate site managers and principal investigators of AERONET sites for offering the datasets used in our study. We sincerely thank Prof. Zhengqiang Li for establishing, maintaining, and managing the SONET network. The authors are also indebted to Drs. Hongqing Liu and Mi Zhou for their assistance with the NOAA/STAR DT algorithm. The materials in this paper only represent the opinions of the authors and do not constitute a statement of decision, policy, or position by NOAA or the U.S. government.

References

Abbot, J. and Marohasy, J., 2012. Application of artificial neural networks to rainfall forecasting in Queensland, Australia. Adv. Atmos. Sci. 29(4), 717–730.

Ackerman, A.S., Kirkpatrick, M.P., Stevens, D.E., Toon, O.B., 2004. The impact of humidity above stratiform clouds on indirect aerosol climate forcing. Nature 432, 1014–1017. https://doi.org/10.1038/nature03174

Boucher, O., Randall, D., Artaxo, P., Bretherton, C., Feingold, G., Forster, P., Kerminen, V.M., Kondo, Y., Liao, H., Lohmann, U., Rasch, P., 2013. Clouds and aerosols, in: Climate Change 2013: The Physical Science Basis. Contribution of Working Group I to the Fifth Assessment Report of the Intergovernmental Panel on Climate Change, 571–657, Cambridge Univ. Press, Cambridge, UK and New York, NY, USA.

Bühlmann, P. and Van De Geer, S., 2011. Statistics for high-dimensional data: methods, theory and applications. Springer Science & Business Media.

Burden, F. and Winkler, D., 2008. Bayesian regularization of neural networks. In Artificial Neural Networks, 23–42.

Chu, D.A., and Coauthors (2002). Validation of MODIS aerosol optical depth retrieval over land. Geophys. Res. Lett. 29(12), 8007. https://doi.org/10.1029/2001GL013205

Chung, C.E., Ramanathan, V., Decremer, D., 2012. Observationally constrained estimates of carbonaceous aerosol radiative forcing. Proc. Natl. Acad. Sci. USA 109(29), 11,624–11,629.

Cireşan, D., Meier, U., Masci, J., Schmidhuber, J., 2012. Multi-column deep neural network for traffic sign classification. Neural Networks 32, 333–338.

Colarco, P., da Silva, A., Chin, M., Diehl, T., 2010. Online simulations of global aerosol distributions in the NASA GEOS‐4 model and comparisons to satellite and ground‐based aerosol optical depth. J. Geophys. Res. Atmos. 115(D14).

Deng, L. and Yu, D., 2014. Deep learning: methods and applications. Foundations and Trends® in Signal Processing 7(3–4), 197–387.

Eck, T.F., Holben, B.N., Reid, J.S., Dubovik, O., Smirnov, A., O'neill, N.T., Slutsker, I., Kinne, S., 1999. Wavelength dependence of the optical depth of biomass burning, urban, and desert dust aerosols. J. Geophys. Res. Atmos. 104(D24), 31,333–31,349.

Gao, B.C. and Kaufman, Y.J., 1995. Selection of the 1.375-μm MODIS channel for remote sensing of cirrus clouds and stratospheric aerosols

–

Gao, B.C., Yang, P., Han, W., Li, R.R., Wiscombe, W.J., 2002. An algorithm using visible and 1.38-μm channels to retrieve cirrus cloud reflectances from aircraft and satellite data. IEEE Trans. Geosci. Remote Sens. 40(8), 1659–1668.

Giles, D., Sinyuk, A., Sorokin, M., Schafer, J., Smirnov, A., Slutsker, I., Eck, T., Holben, B., Lewis, J., Campbell, J., Welton, E., Korkin, S., Lyapustin, A., 2019. Advancements in the Aerosol Robotic Network (AERONET) Version 3 database – automated near real-time quality control algorithm with improved cloud screening for Sun photometer aerosol optical depth (AOD) measurements. Atmos. Meas. Tech. 12, 169–209. https://doi.org/10.5194/amt-12-169-2019

Guo, J., Su, T., Li, Z., Miao, Y., Li, J., Liu, H., Xu, H., Cribb, M., Zhai, P., 2017. Declining frequency of summertime local-scale precipitation over eastern China from 1970 to 2010 and its potential link to aerosols. Geophys. Res. Lett. 44(11), 5700–5708.

Guo, J., Su, T., Chen, D., Wang, J., Li, Z., Lv, Y., Guo, X., Liu, H., Cribb, M., Zhai, P., 2019. Declining summertime local-scale precipitation frequency over China and the United States, 1981–2012: the disparate roles of aerosols. Geophys. Res. Lett. 46(22), 13,281–13,289.

Guo, J., Chen, X., Su, T., Liu, L., Zheng, Y., Chen, D., Li, J., Xu, H., Lv, Y., He, B., Li, Y., 2020. The climatology of lower tropospheric temperature inversions in China from radiosonde measurements: roles of black carbon, local meteorology, and large-scale subsidence. J. Climate, 1–70.

Gupta, P., Levy, R.C., Mattoo, S., Remer, L.A., Munchak, L.A., 2016. A surface reflectance scheme for retrieving aerosol optical depth over urban surfaces in MODIS Dark Target retrieval algorithm. Atmos. Meas. Tech. 9, 3293–3308. https://doi.org/10.5194/amt-9-3293-2016

Gupta, P., Remer, L.A., Levy, R.C., Mattoo, S., 2018. Validation of MODIS 3-km land aerosol optical depth from NASA's EOS Terra and Aqua missions. Atmos. Meas. Tech. 11(5), 3145–3159.

Gupta, P., Levy, R.C., Mattoo, S., Remer, L.A., Holz, R.E., Heidinger, A.K., 2019. Applying the Dark Target aerosol algorithm with Advanced Himawari Imager observations during the KORUS-AQ field campaign. Atmos. Meas. Tech. 12(12), 6557–6577.

Han, W., Li, Z., Wu, F., Zhang, Y., Guo, J., Su, T., Cribb, M., Fan, J., Chen, T., Wei, J.

Lee, S.S., 2020. The mechanisms and seasonal differences of the impact of aerosols on daytime surface urban heat island effect. Atmos. Chem. Phys. 20, 6479–6493.

Haykin, S., 2009. Neural Networks and Learning Machines. 3rd edition, Pearson Education, Inc., New Jersey.

Heidinger, A., Botambekov, D., Walther, A., 2016. A Naïve Bayesian Cloud Mask Delivered to NOAA Enterprise, Algorithm Theoretical Basis Document, Version 1.1, October 14, 2016, (p. 50). Washington, D.C., United States of America: Center for Satellite Applications and Research, National Oceanic and Atmospheric Administration. URL: https://www.star.nesdis.noaa.gov/jpss/documents/ATBD/ATBD_EPS_Cloud_Mask_v1.1.pdf (valid as of August 3, 2020).

Holben, B., Vermote, E., Kaufman, Y.J., Tanré, D., Kalb, V., 1992. Aerosol retrieval over land from AVHRR data-application for atmospheric correction. IEEE Trans. Geosci. Remote Sens. 30(2), 212–222.

Hsu, N.C., Tsay, S.C., King, M.D., Herman, J.R., 2006. Deep blue retrievals of Asian aerosol properties during ACE-Asia. IEEE Trans. Geosci. Remote Sens. 44(11), 3180–3195.

Hsu, N.C., Jeong, M.J., Bettenhausen, C., Sayer, A.M., Hansell, R., Seftor, C.S., Huang, J., Tsay, S.C., 2013. Enhanced Deep Blue aerosol retrieval algorithm: The second generation. J. Geophys. Res. Atmos. 118(16), 9296–9315.

Imai, T. and Yoshida, R., 2016. Algorithm Theoretical Basis for Himawari-8 Cloud

Mask Product. Meteorological Satellite Center Technical Note, 61, 1–17.

Jackson, J.M., Liu, H., Laszlo, I., Kondragunta, S., Remer, L.A., Huang, J., Huang, H.C., 2013. Suomi-NPP VIIRS aerosol algorithms and data products. J. Geophys. Res. Atmos. 118(22), 12–673.

Jeong, M.-J., Li, Z., Chu, D.A., Tsay, S.-C., 2005. Quality and compatibility analyses of global aerosol products derived from the advanced very high resolution radiometer and Moderate Resolution Imaging Spectroradiometer. J. Geophys. Res. Atmos. 110, D10S09. https://doi.org/10.1029/2004JD004648

Kahn, R.A., Nelson, D.L., Garay, M.J., Levy, R.C., Bull, M.A., Diner, D.J., Martonchik, J.V., Paradise, S.R., Hansen, E.G., Remer, L.A., 2009. MISR aerosol product attributes and statistical comparisons with MODIS. IEEE Trans. Geosci. Remote Sens. 47(12), 4095–4114.

Kahn, R.A., Berkoff, T.A., Brock, C., Chen, G., Ferrare, R.A., Ghan, S., Hansico, T.F., Hegg, D.A., Martins, J.V., McNaughton, C.S., Murphy, D.M., 2017. SAM-CAAM: a concept for acquiring systematic aircraft measurements to characterize aerosol air masses. 98(10), 2215–2228.

Kaufman, Y.J. and Remer, L.A., 1994. Detection of forests using mid-IR reflectance: an application for aerosol studies. IEEE Trans. Geosci. Remote Sens. 32(3), 672–683.

Kaufman, Y. J., and Coauthors, 1997a. Operational remote sensing of tropospheric aerosol over land from EOS moderate resolution imaging spectroradiometer. J.

Geophys. Res 102(D14), 17,051–17,067.

Kaufman, Y.J., Wald, A.E., Remer, L.A., Gao, B.C., Li, R.R., Flynn, L., 1997b. The MODIS 2.1 μm channel-correlation with visible reflectance for use in remote sensing of aerosol. IEEE Trans. Geosci. Remote Sens. 35, 1286–1298.

Kaufman, Y. J., and Coauthors, 2002. Relationship between surface reflectance in the visible and mid-IR used in MODIS aerosol algorithm: theory. Geophys. Res. Lett. 29(23).

Kaufman, Y. J., and Coauthors, 2005. Aerosol anthropogenic component estimated from satellite data. Geophys. Res. Lett. 32, L17804, https://doi.org/10.1029/2005GL023125.

Kim, J., Yoon, J.M., Ahn, M.H., Sohn, B.J., Lim, H.S., 2008. Retrieving aerosol optical depth using visible and mid-IR channels from geostationary satellite MTSAT-1R. Int. J. Remote Sens., 29(21), 6181–6192.

Kim, J., Jeong, U., Ahn, M.H., Kim, J.H., Park, R.J., Lee, H., Song, C.H., Choi, Y.S., Lee, K.H., Yoo, J.M., Jeong, M.J., 2019. New era of air quality monitoring from space: Geostationary Environment Monitoring Spectrometer (GEMS). 101, E1-E22.

King, M.D., Kaufman, Y.J., Tanré, D., Nakajima, T., 1999. Remote sensing of tropospheric aerosols from space: past, present and future. Bull. Am. Meteorol. Soc. 80, 2229–2259.

King, M.D., Menzel, W.P., Kaufman, Y.J., Tanré, D., Gao, B.-C., Platnick, S., Ackerman, S.A., Remer, L.A., Pincus, R., Hubanks, P.A., 2003. Cloud and aerosol properties, precipitable water, and profiles of temperature and humidity from MODIS. IEEE Trans. Geosci. Remote Sens. 41, 442–458. https://doi.org/10.1029/2006JD007811

Kobayashi, H., Suzuki, R., Kobayashi, S., 2007. Reflectance seasonality and its relation to the canopy leaf area index in an eastern Siberian larch forest: multi-satellite data and radiative transfer analyses. Remote Sens. Environ. 106(2), 238–252.

Laszlo, I. (2018). Remote Sensing of Tropospheric Aerosol Optical Depth From Multispectral Monodirectional Space-Based Observations, in *Comprehensive Remote Sensing*, edited by S. Liang, pp. 137–196, Elsevier, Oxford, https://doi.org/10.1016/B978-0-12-409548-9.10389-6.

Laszlo, I., Ciren, P., Liu, H.Q., Kondragunta, S., Tarpley, J.D., Goldberg, M.D. (2008). Remote sensing of aerosol and radiation from geostationary satellites. Adv. Space Res. 41(11), 1882–1893. https://doi.org/10.1016/j.asr.2007.06.047

Laszlo, I., Liu, H., Kim, H.Y., Pinker, R.T., 2020. Shortwave Radiation from ABI on the GOES-R Series. In The GOES-R Series (pp. 179–191). Elsevier.

Levy, R. C., and Coauthors, 2005. Evaluation of the MODIS aerosol retrievals over ocean and land during CLAMS. J. Atmos. Sci., 62(4), 974–992.

Levy, R. C., and Coauthors, 2007a. Global aerosol optical properties and application to MODIS aerosol retrieval over land. J. Geophys. Res. Atmos. 112, D13210. https://doi.org/10.1029/2006JD007815

Levy, R.C., Remer, L.A., Mattoo, S., Vermote, E.F., Kaufman, Y.J., 2007b. Second-generation operational algorithm: retrieval of aerosol properties over land from inversion of Moderate Resolution Imaging Spectroradiometer spectral reflectance. J. Geophys. Res. Atmos. 112(D13).

Levy, R., Mattoo, S., Munchak, L.A., Remer, L.A., Sayer, A.M., Patadia, F., Hsu, N.C., 2013. The Collection 6 MODIS aerosol products over land and ocean. Atmos. Meas. Tech. 6, 2989–3034. https://doi.org/10.5194/amt-6-2989-2013

Li, C., Li, J., Dubovik, O., Zeng, Z.C., Yung, Y.L., 2020. Impact of aerosol vertical distribution on aerosol optical depth retrieval from passive satellite sensors. Remote Sens. 12(9), 1524. https://doi.org/10.3390/rs12091524

Li, J., Carlson, B.E., Lacis, A.A., 2013. Application of spectral analysis techniques in the intercomparison of aerosol data: 1. An EOF approach to analyze the spatial-temporal variability of aerosol optical depth using multiple remote sensing data sets. J. Geophys. Res. Atmos. 118(15), 8640–8648.

Li, J., Carlson, B.E., Dubovik, O., Lacis, A.A., 2014. Recent trends in aerosol optical properties derived from AERONET measurements. Atmos. Chem. Phys. 14(22), 12,271–12,289.

Li, J., Carlson, B.E.,Lacis, A.A., 2015. How well do satellite AOD observations represent the spatial and temporal variability of $PM_{2.5}$ concentration for the United States?. Atmos. Environ. 102, 260–273.

Li, Z., Zhao, X., Kahn, R., Mishchenko, M., Remer, L., Lee, K.-H., Wang, M., Laszlo, I., Nakajima, T., Maring, H., 2009. Uncertainties in satellite remote sensing of aerosols and impact on monitoring its long-term trend: a review and perspective. Ann. Geophys. 27, 2755–2770.

Li, Z., Niu, F., Fan, J., Liu, Y., Rosenfeld, D., Ding, Y., 2011. Long-term impacts of aerosols on the vertical development of clouds and precipitation. Nature Geosci. 4(12), 888.

Li, Z., Rosenfeld, D., Fan, J., 2017. Aerosols and their impact on radiation, clouds, precipitation and severe weather events. Oxford Encyclopedia of Environmental Sciences, https://doi.org/10.1093/acrefore/9780199389414.013.126, 2017.

Li, Z., Xu, H., Li, K., Li, D., Xie, Y., Li, L., Zhang, Y., Gu, X., Zhao, W., Tian, Q., Deng, R., Su, X., Huang, B., Qiao, Y., Cui, W., Hu, Y., Gong, C., Wang, Y., Wang, X., Wang, J., Du, W., Pan, Z., Li, Z., Bu, D., 2018. Comprehensive study of optical, physical, chemical, and radiative properties of total columnar atmospheric aerosols over China: an overview of Sun–Sky Radiometer Observation Network (SONET) measurements. Bull. Amer. Meteorol. Soc. 99, 739–755. https://doi.org/10.1175/BAMSD-17-0133.1

Lin, C., Li, Y., Yuan, Z., Lau, A.K., Li, C., Fung, J.C., 2015. Using satellite remote sensing data to estimate the high-resolution distribution of ground-level $PM_{2.5}$.

Remote Sens. Environ. 156, 117–128.

Lin, C., Li, Y., Lau, A.K., Deng, X., Tim, K.T., Fung, J.C., Li, C., Li, Z., Lu, X., Zhang, X., Yu, Q., 2016. Estimation of long-term population exposure to $PM_{2.5}$ for dense urban areas using 1-km MODIS data. Remote Sens. Environ. 179, 13–22.

Liu, N., Zou, B., Feng, H., Wang, W., Tang, Y., Liang, Y., 2019. Evaluation and comparison of multiangle implementation of the atmospheric correction algorithm, Dark Target, and Deep Blue aerosol products over China. Atmos. Chem. Phys. 19, 8243–8268.

Liu, W., Wang, Z., Liu, X., Zeng, N., Liu, Y., Alsaadi, F.E., 2017. A survey of deep neural network architectures and their applications. Neurocomputing 234, 11–26.

Lyapustin, A., Martonchik, J., Wang, Y., Laszlo, I., Korkin, S., 2011. Multiangle implementation of atmospheric correction (MAIAC): 1. Radiative transfer basis and look-up tables. J. Geophys. Res. Atmos. 116(D3).

Lyapustin, A., Wang, Y., Korkin, S., Huang, D., 2018. MODIS Collection 6 MAIAC algorithm. Atmos. Meas. Tech. 11(10).

Ma, R., Letu, H., Yang, K., Wang, T., Shi, C., Xu, J., Shi, J., Shi, C., Chen, L., 2020. Estimation of surface shortwave radiation from Himawari-8 satellite data based on a combination of radiative transfer and deep neural network. IEEE Trans. Geosci. Remote Sens. 58(8), 5304–5316.

Mhawish, A., Banerjee, T., Broday, D.M., Misra, A., Tripathi, S.N., 2017. Evaluation of

MODIS Collection 6 aerosol retrieval algorithms over Indo-Gangetic Plain: implications of aerosols types and mass loading. Remote Sens. Environ. 201, 297–313.

Mhawish, A., Kumar, M., Mishra, A.K., Srivastava, P.K., Banerjee, T., 2018. Remote sensing of aerosols from space: retrieval of properties and applications. In: Remote Sensing of Aerosols, Clouds, and Precipitation. Elsevier Inc, pp. 1–38. https://doi.org/10.1016/B978-0-12-810437-8.00003-7

Mhawish, A., Banerjee, T., Sorek-Hamer, M., Lyapustin, A., Broday, D.M., Chatfield, R., 2019. Comparison and evaluation of MODIS multi-angle implementation of atmospheric correction (MAIAC) aerosol product over South Asia. Remote Sens. Environ. 224, 12–28.

Mielonen, T., Levy, R.C., Aaltonen, V., Komppula, M., De Leeuw, G., Huttunen, J., Lihavainen, H., Kolmonen, P., Lehtinen, K.E.J., Arola, A., 2011. Evaluating the assumptions of surface reflectance and aerosol type selection within the MODIS aerosol retrieval over land: the problem of dust type selection. Atmos. Meas. Tech. 4, 201–214.

Montavon, G., Samek, W., Müller, K.-R., 2017. Methods for interpreting and understanding deep neural networks. Digit. Signal Process. 73, 1–15.

Ramanathan, V.C.P.J., Crutzen, P.J., Kiehl, J.T., Rosenfeld, D., 2001. Aerosols, climate, and the hydrological cycle. Science 294(5549), 2119–2124.

Reichstein, M., Camps-Valls, G., Stevens, B., Jung, M., Denzler, J., Carvalhais, N., 2019. Deep learning and process understanding for data-driven Earth system science. Nature 566(7743), 195–204.

Remer, L. A., and Coauthors (2001). Angular and seasonal variation of spectral surface reflectance ratios: implications for the remote sensing of aerosol over land. IEEE Trans. Geosci. Remote Sens. 39(2), 275–283.

Remer, L.A., Kaufman, Y.J., Tanré, D., Mattoo, S., Chu, D.A., Martins, J.V., Li, R.R., Ichoku, C., Levy, R.C., Kleidman, R.G., Eck, T.F., Vermote, E., Holben, B.N. (2005). The MODIS aerosol algorithm, products, and validation. J. Atmos. Sci. 62, 947–973.

Remer, L.A., Tanré, D., Kaufman, Y.J., Levy, R., Mattoo, S., 2006. Algorithm for remote sensing of tropospheric aerosol from MODIS: Collection 5, Product ID MOD04/MYD04.

Remer, L.A., Kleidman, R.G., Levy, R.C., Kaufman, Y.J., Tanré, D., Mattoo, S., Martins, J.V., Ichoku, C., Koren, I., Yu, H., Holben, B.N., 2008. Global aerosol climatology from the MODIS satellite sensors. J. Geophys. Res. Atmos. 113(D14).

Remer, L.A., Mattoo, S., Levy, R.C., Munchak, L.A., 2013. MODIS 3-km aerosol product: algorithm and global perspective. Atmos. Meas. Tech. 6, 1829–1844.

Rodriguez, J.D., Perez, A., Lozano, J.A., 2010. Sensitivity analysis of k-fold cross validation in prediction error estimation. IEEE Trans. Pattern Anal. Mach. Intell. 32(3), 569–575.

Runge, J., Petoukhov, V., Donges, J.F., Hlinka, J., Jajcay, N., Vejmelka, M., Hartman, D., Marwan, N., Paluš, M., Kurths, J., 2015. Identifying causal gateways and mediators in complex spatio-temporal systems. Nature Commun. 6(1), 1–10.

https://doi.org/10.1038/ncomms9502

Sarle, Warren S., 1994. Neural networks and statistical models, Proc. 19th Annual SAS Users Group Int. Conf., Cary, NC, April 1994, 1538–1550.

Schmidhuber, J., 2015. Deep learning in neural networks: an overview. Neural Netw. 61, 85–117.

Seide, F., Li, G. Yu, D., 2011. Conversational speech transcription using context-dependent deep neural networks. In: Twelfth annual conference of the international speech communication association.

Sheela, K.G. and Deepa, S.N., 2013. Review on methods to fix number of hidden neurons in neural networks. Math. Probl. Eng. 2013. https://doi.org/10.1155/2013/425740

Stan, O. and Kamen, E.W., 1999. New block recursive MLP training algorithms using the Levenberg–Marquardt algorithm, in: International Joint Conference on Neural Networks, 10–16 July, vol. 3, pp. 1672–1677.

Su, T., Li, J., Li, C., Lau, A.K.H., Yang, D., Shen, C., 2017. An intercomparison of AOD-converted $PM_{2.5}$ concentrations using different approaches for estimating aerosol vertical distribution. Atmos. Environ. 166, 531–542.

Su, T., Li, Z., Kahn, R., 2018. Relationships between the planetary boundary layer height and surface pollutants derived from lidar observations over China: regional pattern and influencing factors. Atmos. Chem. Phys. 18(21), 15,921–15,935.

Su, T., Li, Z., Kahn, R., 2020a. A new method to retrieve the diurnal variability of planetary boundary layer height from lidar under different thermodynamic stability conditions. Remote Sens. Environ. 237, 111519.

Su, T., Li, Z., Li, C., Li, J., Han, W., Shen, C., Tan, W., Guo, J., 2020b. The significant impact of aerosols vertical structure on lower-atmosphere stability and its critical role in aerosol–PBL interaction. Atmos. Chem. Phys. 20, 3713–3724. https://doi.org/10.5194/acp-20-3713-2020

Tirelli, C., Curci, G., Manzo, C.,Tuccella, P., Bassani, C., 2015. Effect of the aerosol model assumption on the atmospheric correction over land: case studies with CHRIS/PROBA hyperspectral images over Benelux. Remote Sens. 7, 8391–8415. https://doi.org/10.3390/rs70708391

Tong, W., Li, L., Zhou, X., Hamilton, A., Zhang, K., 2019. Deep learning $PM_{2.5}$ concentrations with bidirectional LSTM RNN. Air Qual. Atmos. Hlth. 12(4), 411–423.

Van Donkelaar, A., Martin, R.V., Park, R.J., 2006. Estimating ground-level $PM_{2.5}$ using aerosol optical depth determined from satellite remote sensing. J. Geophys. Res. Atmos. 111(D21).

Vermote, E.F., Tanré, D., Deuze, J.L., Herman, M., Morcette, J.J., 1997a. Second simulation of the satellite signal in the solar spectrum, 6S: an overview. IEEE Trans. Geosci. Remote Sens. 35(3), 675–686.

Vermote, E.F., El Saleous, N., Justice, C.O., Kaufman, Y.J., Privette, J.L., Remer, L., Roger, J.C., Tanré, D., 1997b. Atmospheric correction of visible to middle-infrared

EOS-MODIS data over land surfaces: background, operational algorithm and validation. J. Geophys. Res. Atmos. 102(D14), 17,131–17,141.

Vermote, E.F., El Saleous, N.Z., Justice, C.O., 2002. Atmospheric correction of MODIS data in the visible to middle infrared: first results. Remote Sens. Environ. 83(1–2), 97–111.

Walton, C.C., Pichel, W.G., Sapper, J.F., May, D.A., 1998. The development and operational application of nonlinear algorithms for the measurement of sea surface temperatures with the NOAA polar-orbiting environmental satellites. J. Geophys. Res. Atmos. 103(C12), 27,999–28,012. https://doi.org/10.1029/98JC02370

Wang, W., Pan, Z., Mao, F., Gong, W., Shen, L., 2017. Evaluation of VIIRS land aerosol model selection with AERONET measurements. Int. J. Environ. Res. Public Hlth. 14, 1016. https://doi.org/10.3390/ijerph14091016

Wei, J., Sun, L., Peng, Y., Wang, L., Zhang, Z., Bilal, M., Ma, Y., 2018. An improved high spatial-resolution aerosol retrieval algorithm for MODIS images over land. J. Geophys. Res. Atmos. 123, 12,291–12,307. https://doi.org/10.1029/2017JD027795

Wei, J., Huang, W., Li, Z., Xue, W., Peng, Y., Sun, L., Cribb, M., 2019a. Estimating 1-km-resolution $PM_{2.5}$ concentrations across China using the space-time random forest approach. Remote Sens. Environ. 231, 111221. https://doi.org/10.1016/j.rse.2019.111221

Wei, J., Li, Z., Guo, J., Sun, L., Huang, W., Xue, W., Fan, T., Cribb, M., 2019b. Satellite-derived 1-km-resolution PM_1 concentrations from 2014 to 2018 across China.

Environ. Sci. Tech. 53(22), 13,265–13,274.

Wei, J., Li, Z., Peng, Y., Sun, L., 2019c. MODIS Collection 6.1 aerosol optical depth products over land and ocean: validation and comparison. Atmos. Environ. 201, 428–440.

Wei, J., Li, Z., Sun, L., Peng, Y., Zhang, Z., Li, Z., Su, T., Feng, L., Cai, Z., Wu, H., 2019d. Evaluation and uncertainty estimate of next-generation geostationary meteorological Himawari-8/AHI aerosol products. Sci. Total Environ. 692, 879–891.

Wei, J., Li, Z., Cribb, M., Huang, W., Xue, W., Sun, L., Guo, J., Peng, Y., Li, J., Lyapustin, A., Liu, L., Wu, H., Song, Y., 2020. Improved 1-km resolution $PM_{2.5}$ estimates across China using enhanced space-time extremely randomized trees, Atmos. Chem. Phys. 20(6), 3273–3289.

Wu, Y., de Graaf, M., Menenti, M., 2016. The sensitivity of AOD retrieval to aerosol type and vertical distribution over land with MODIS data. Remote Sens. 8, 765.

Yoshida, M., Kikuchi, M., Nagao, T., Murakami, H., Nomaki, T., Higurashi, A., 2018. Common retrieval of aerosol properties for imaging satellite sensors. J. Meteorol. Soc. Japan 96b, 193–209. https://doi.org/10.2151/jmsj.2018-039

Yu, H., and Coauthors, 2006. A review of measurement-based assessments of aerosol direct radiative effect and forcing. Atmos. Chem. Phys. 6, 613–666.

Zhang, Q.S. and Zhu, S.C., 2018. Visual interpretability for deep learning: a survey. Front. Inform. Tech. El. 19(1), 27–39.

Zhang, Z., Wu, W., Fan, M., Tao, M., Wei, J., Jin, J., Tan, Y., Wang, Q., 2019. Validation of Himawari-8 aerosol optical depth retrievals over China. Atmos. Environ. 199, 32–44.

List of Tables

Table 1. Empirical functions relating surface reflectances (*SR*) at 0.47, 0.64, and 2.25 μm. Θ indicates the scattering angle. $NDVI_{SWIR}$ is the shortwave infrared normalized difference vegetation index.

$\boldsymbol{NDVI_{SWIR}}$ **range**	$\boldsymbol{SR_{0.64} = m + n \times SR_{2.25}}$ $\boldsymbol{m = a + b \times \Theta;\ \ n = c + d \times \Theta}$ $\boldsymbol{SR_{0.47} = 0.86 \times SR_{0.64} - 0.02}$ ***a***	***b***	***c***	***d***
$NDVI_{SWIR}$<0.2	-0.0416	0.00058	0.68	-0.00095
0.2≤ $NDVI_{SWIR}$<0.3	-0.038	0.00060	0.9	-0.0036
0.3≤ $NDVI_{SWIR}$<0.4	-0.026	0.00026	1.21	
0.4≤ $NDVI_{SWIR}$<0.5	-0.0147	0.000067	1.32	
0.5≤ $NDVI_{SWIR}$	0.0077	-0.00011	0.91	

Table 2. Classification of different regions for independent tests.

Region code	Classification	Number of sites
R1	Latitude > 23^{o}N	9
R2	Latitude < 23^{o}N	9
L1	Longitude > 110^{o}E	12
L2	Longitude < 110^{o}E	6

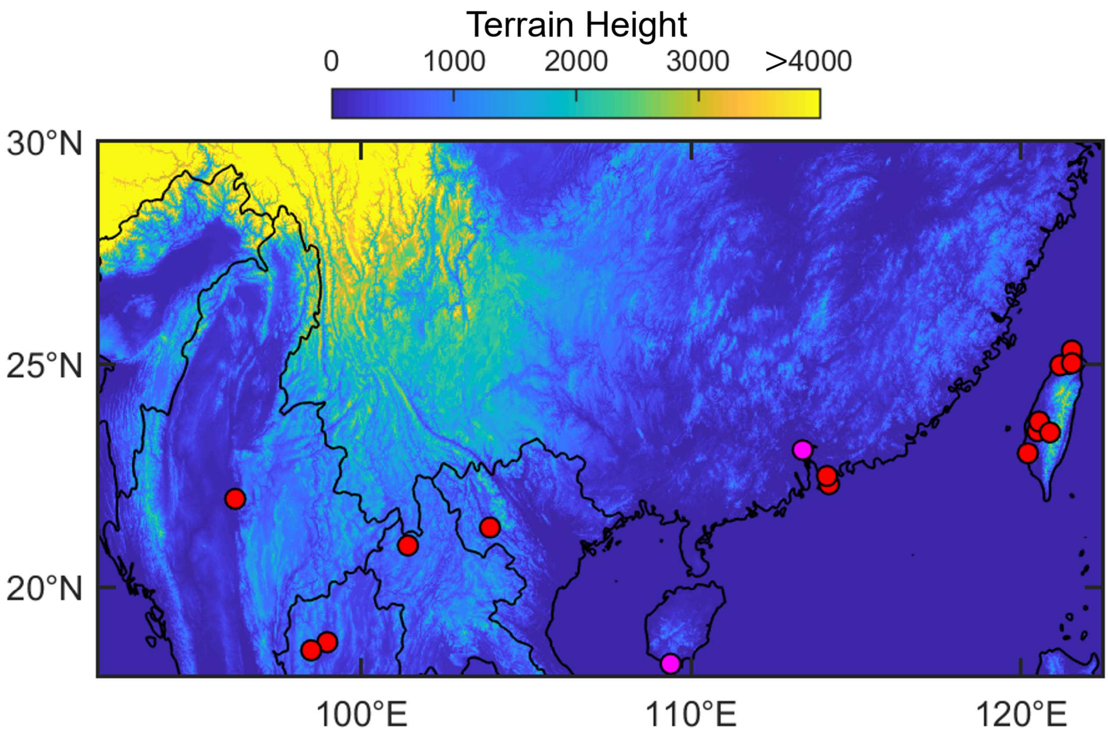

Fig. 1. Spatial distribution of terrain height (unit: m) of the study region. Red dots indicate the 16 AERONET sites, and pink dots indicate the 2 SONET sites used in our study.

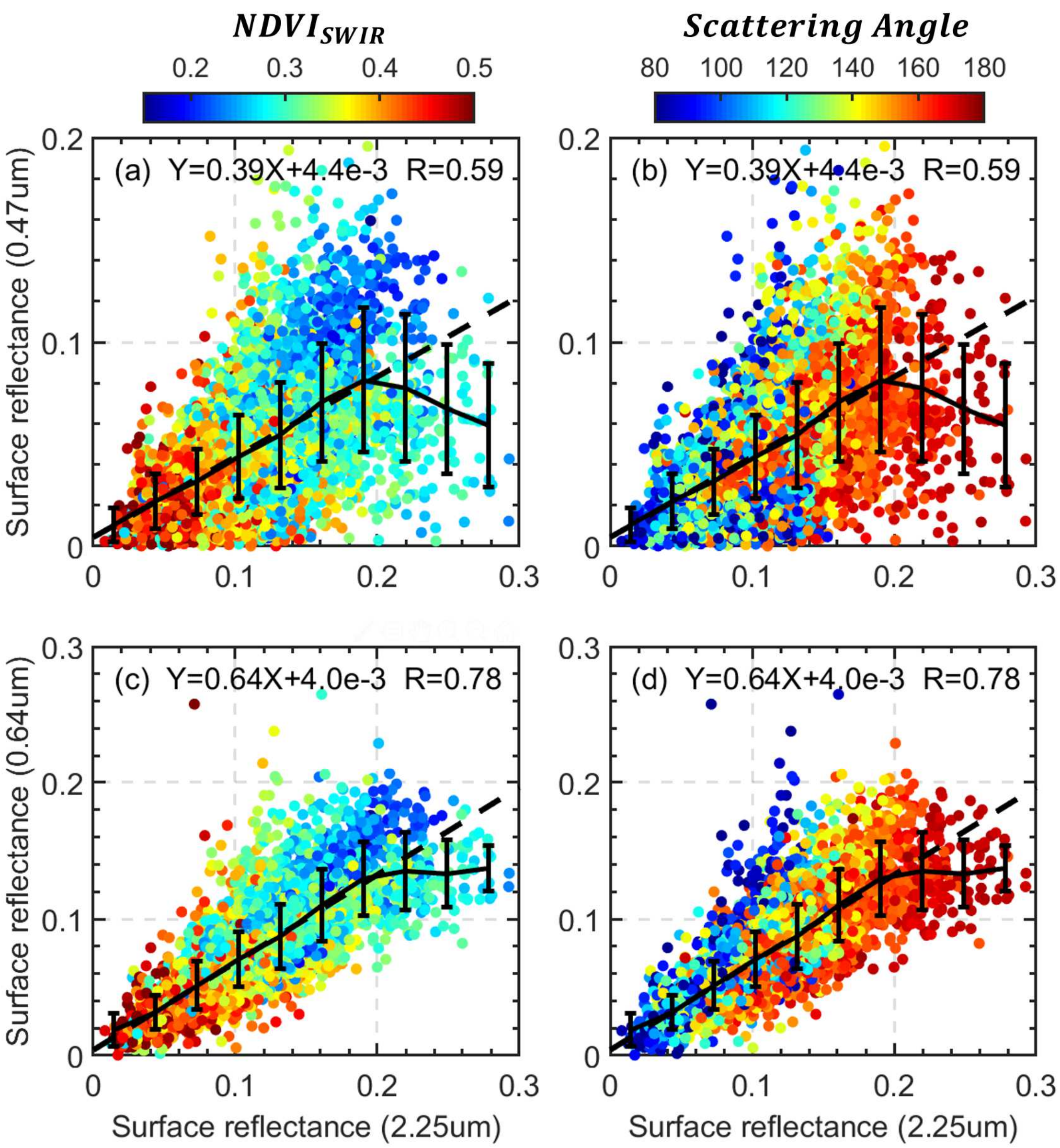

Fig. 2. (a, b) The linear regression between $SR_{0.47}$ (surface reflectance at 0.47 μm) and $SR_{2.25}$ (surface reflectance at 2.25 μm). (c, d) The linear regression between $SR_{0.64}$ (surface reflectance at 0.64 μm) and $SR_{2.25}$. In (a, c), the color-shaded dots indicate the corresponding $NDVI_{SWIR}$. In (b, d), the color-shaded dots indicate the corresponding scattering angle. The black solid lines and error bars represent the average values and standard deviations for each bin, which divides the x-axis into ten equal parts. The regression equations and correlation coefficients (R) are given at the top of each panel. The SR data are derived from matched ground AOD and AHI data.

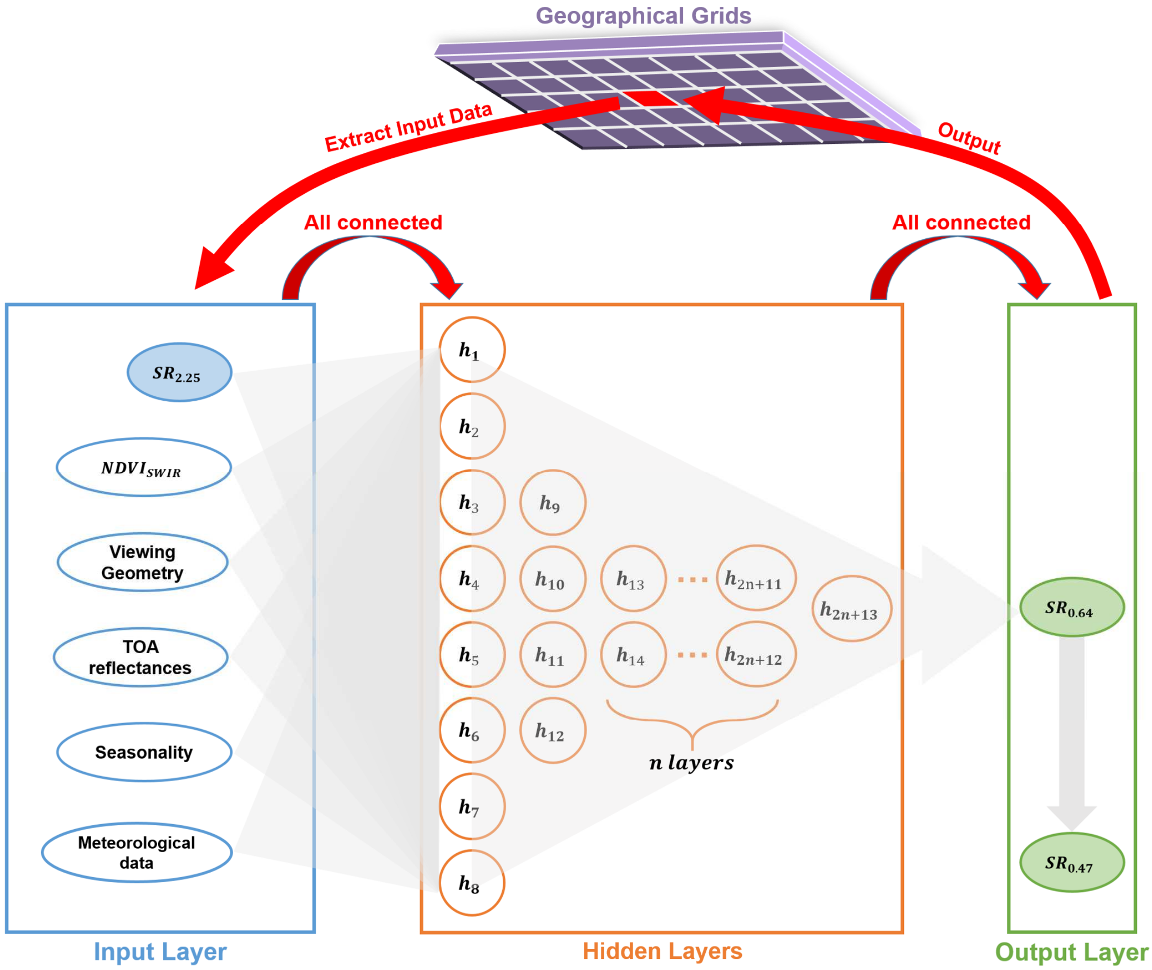

Fig. 3. Diagram describing the deep neural network (DNN) used to derive $SR_{0.64}$. $SR_{0.47}$ is calculated from $SR_{0.64}$, based on a simple linear function (Table 1).

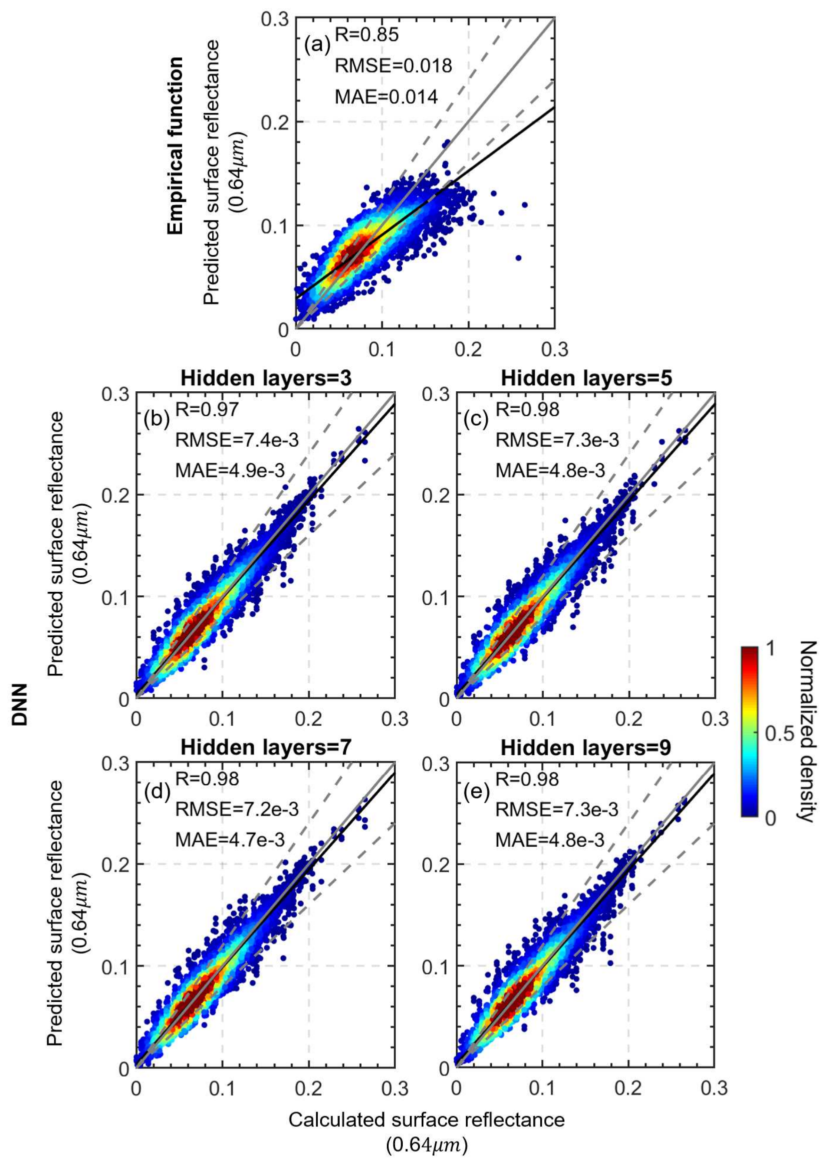

Fig. 4. (a) Density scatterplots of the comparison between surface reflectance (*SR*) at 0.64 μm ($SR_{0.64}$) predicted by the empirical function and $SR_{0.64}$ calculated from Eqs. 1–3, the "true" surface reflectance. (b-e) Density scatterplots of 10-cross-validation results for $SR_{0.64}$ derived from DNN, considering different numbers of hidden layers in the DNN model. The correlation coefficients (R), root-mean-square errors (RMSE), and mean absolute errors (MAE) are given in each panel. The solid black lines represent the best-fit lines from linear regression. The dashed grey lines are plotted as Y=0.8X and Y=1.2X (positions of 20% error).

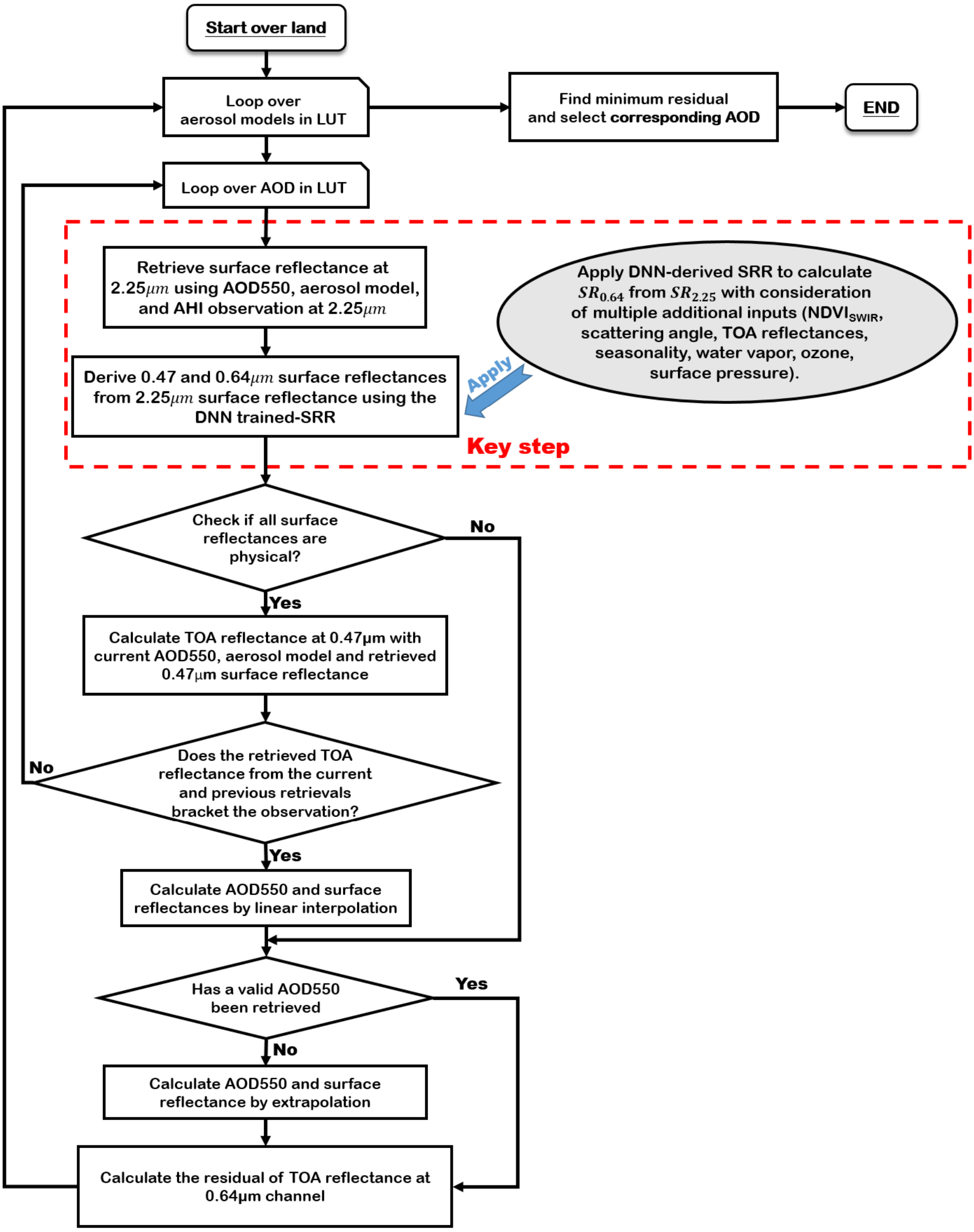

Fig. 5. Flowchart of the DTDL algorithm for retrieving AOD for clear pixels over land. The modules enclosed by the red, dashed lines represent updates the DTDL algorithm introduced into the NOAA/STAR DT algorithm.

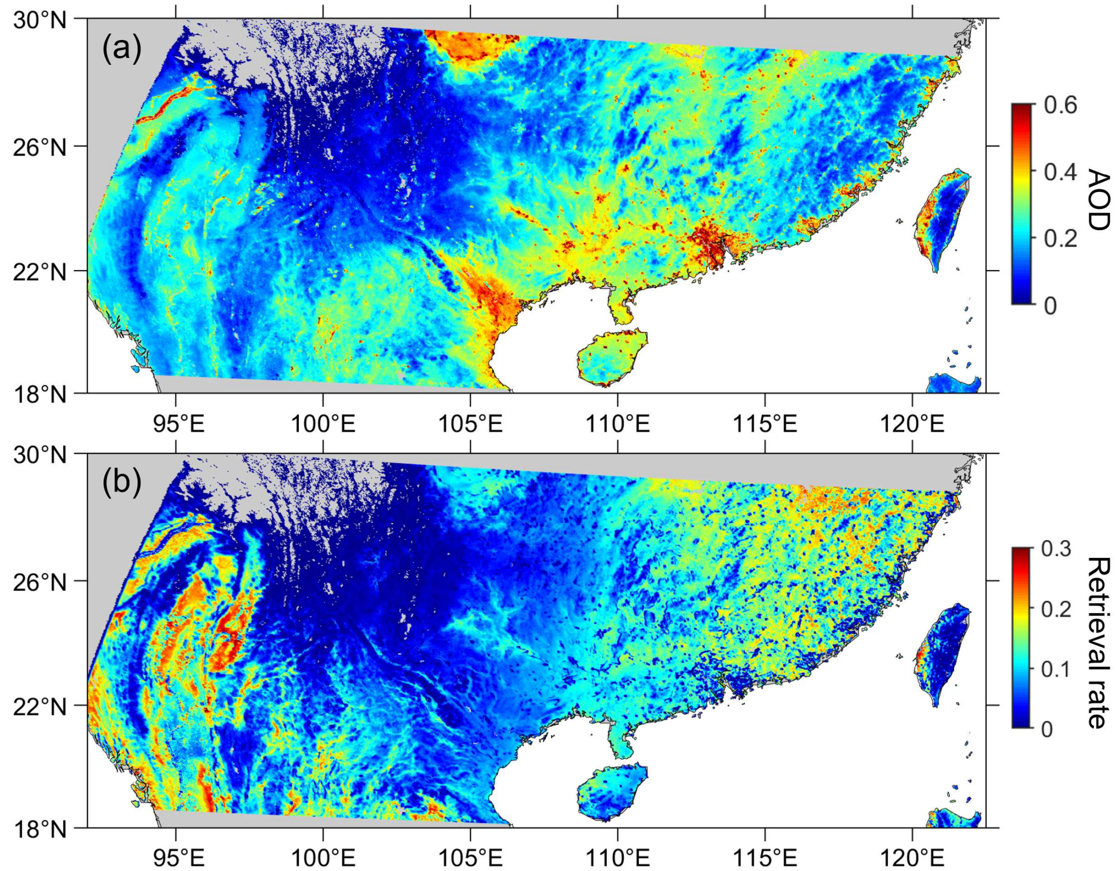

Fig. 6. Spatial distributions of (a) mean aerosol optical depth (AOD) and (b) available retrieval rate derived from the DTDL algorithm for the year 2017.

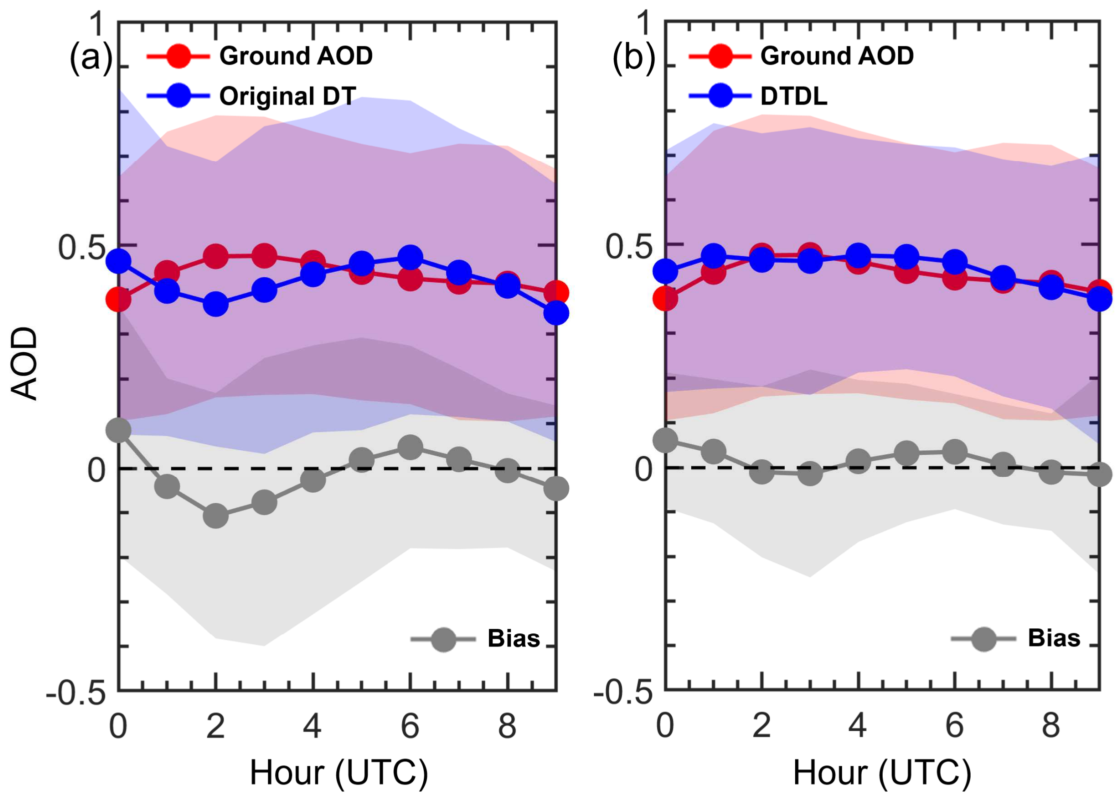

Fig. 7. Diurnal variation in Himawari-8/AHI AOD retrievals derived from (a) the original DT and (b) the DTDL algorithms for the year 2017. Here, all matched pairs of AHI retrievals and ground measurements are used. The diurnal variation derived from ground-based measurements is shown in red, and the bias between AHI and ground AODs is shown in grey. The shaded areas represent the standard deviations.

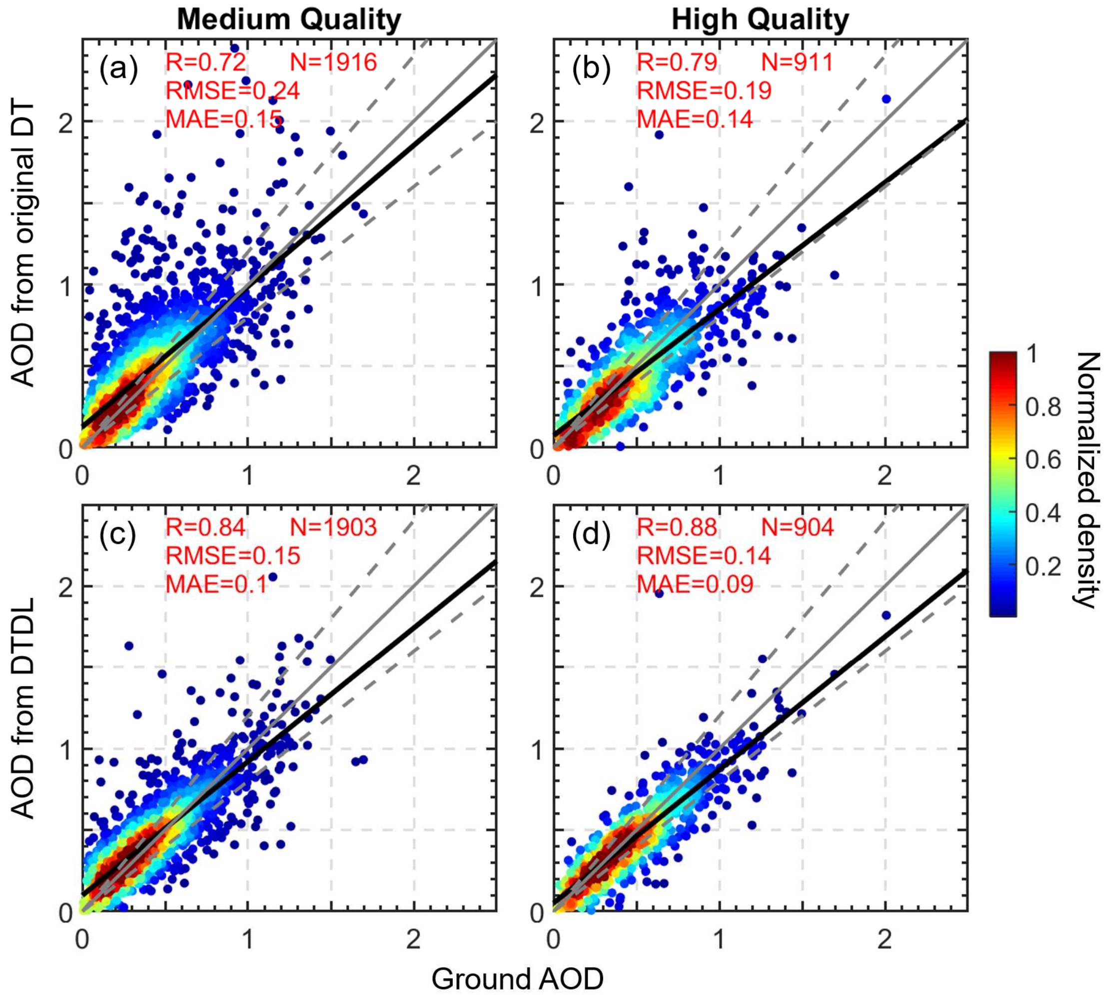

Fig. 8. Comparisons between AERONET AOD and AOD derived from the original DT method for (a) medium-quality and (b) high-quality data for the year 2017. Comparisons between AERONET AOD and AOD derived from the DTDL method for (c) medium-quality and (d) high-quality data for the year 2017. The dashed grey lines are plotted as Y=0.8X and Y=1.2X (positions of 20% error). The correlation coefficients (R), root-mean-square errors (RMSE), number of samples (N), and mean absolute errors (MAE) are given in each panel.

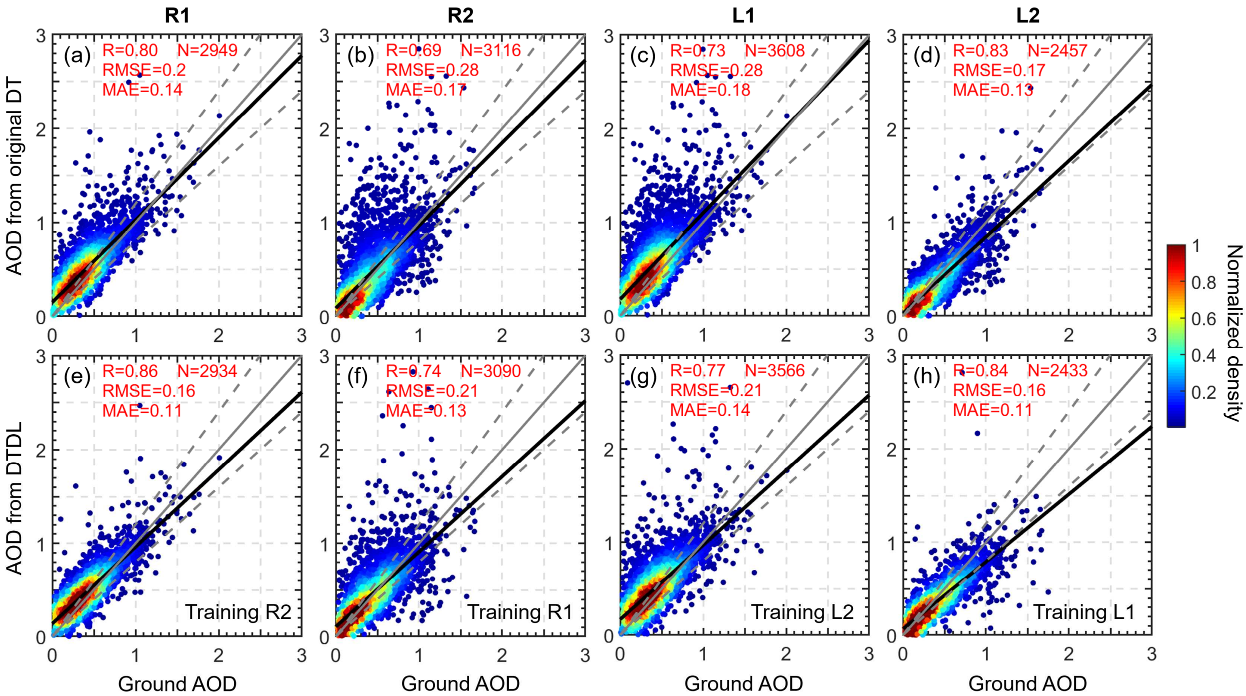

Fig. 9. Comparisons between AERONET AOD and AOD derived from the original DT method for regions (a) R1, (b) R2, (c) L1, and (d) L2. Comparisons between AERONET AOD and AOD derived from the DTDL algorithm for regions (e) R1, (f) R2, (g) L1, and (h) L2, with the training datasets obtained over regions (e) R2, (f) R1, (g) L2, and (h) L1. This process ensures independence of the validation datasets. The dashed grey lines are plotted as Y=0.8X and Y=1.2X (positions of 20% error). The correlation coefficients (R), root-mean-square errors (RMSE), number of samples (N), and mean absolute errors (MAE) are given in each panel.

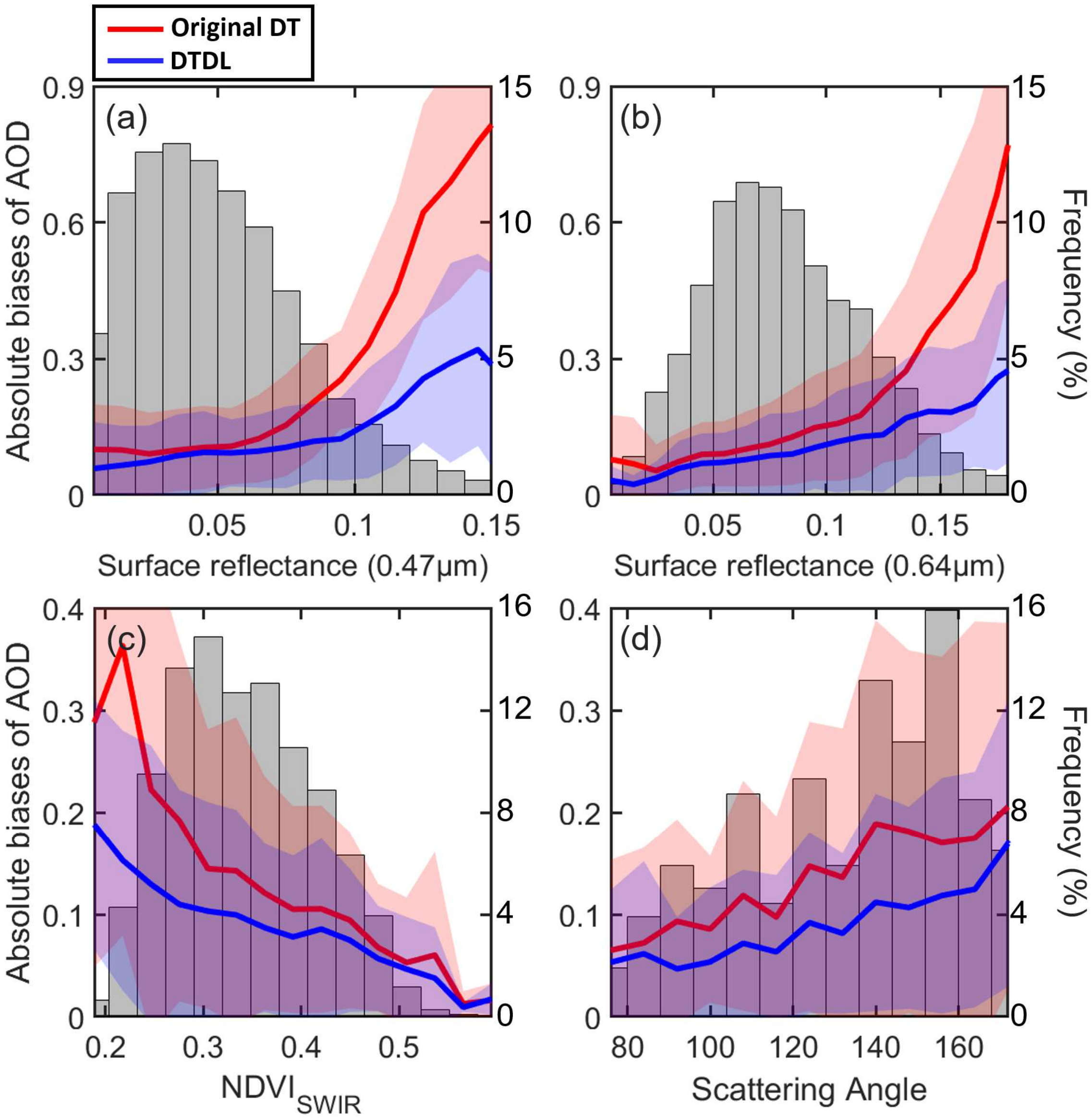

Fig. 10. Absolute biases between AOD derived from ground measurements and retrieved from AHI in 2017 for different (a) $SR_{0.47}$, (b) $SR_{0.64}$, (c) $NDVI_{SWIR}$, and (d) scattering angles. The original DT (red lines) and DTDL (blue lines) algorithms are used. The shaded areas indicate standard deviations. The grey bars represent the frequency of occurrence of these parameters.